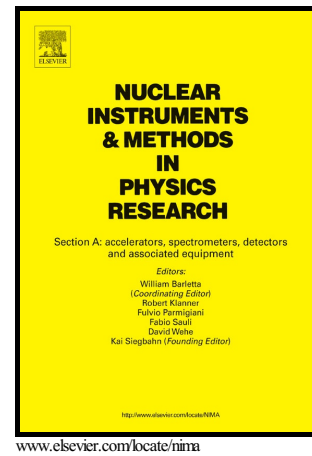


Author's Accepted Manuscript

Fast neutron tomography with real-time pulse-shape discrimination in organic scintillation detectors

Malcolm J. Joyce, Stewart Agar, Michael D. Aspinall, Jonathan S. Beaumont, Edmund Colley, Miriam Colling, Joseph Dykes, Phoivos Kardasopoulos, Katie Mitton



PII: S0168-9002(16)30794-X
DOI: <http://dx.doi.org/10.1016/j.nima.2016.07.044>
Reference: NIMA59218

To appear in: *Nuclear Inst. and Methods in Physics Research, A*

Received date: 18 April 2016
Revised date: 17 July 2016
Accepted date: 24 July 2016

Cite this article as: Malcolm J. Joyce, Stewart Agar, Michael D. Aspinall, Jonathan S. Beaumont, Edmund Colley, Miriam Colling, Joseph Dykes, Phoivos Kardasopoulos and Katie Mitton, Fast neutron tomography with real-time pulse shape discrimination in organic scintillation detectors, *Nuclear Inst. and Methods in Physics Research, A*, <http://dx.doi.org/10.1016/j.nima.2016.07.044>

This is a PDF file of an unedited manuscript that has been accepted for publication. As a service to our customers we are providing this early version of the manuscript. The manuscript will undergo copyediting, typesetting, and review of the resulting galley proof before it is published in its final citable form. Please note that during the production process errors may be discovered which could affect the content, and all legal disclaimers that apply to the journal pertain.

Fast Neutron Tomography with Real-time Pulse-Shape Discrimination in Organic Scintillation Detectors

Malcolm J. Joyce^{a,*}, Stewart Agar^a, Michael D. Aspinall^b, Jonathan S. Beaumont^a, Edmund Colley^a, Miriam Colling^a, Joseph Dykes^a, Phoivos Kardasopoulos^a, Katie Mitton^a

^aDepartment of Engineering, Lancaster University, Lancaster, Lancashire, LA1 4YW, United Kingdom.

^bHybrid Instruments Ltd., Gordon Manley Building, Lancaster Environment Centre, Lancaster University, Lancaster, LA1 4YW, United Kingdom.

*Corresponding author: m.joyce@lancaster.ac.uk

Abstract

A fast neutron tomography system based on the use of real-time pulse-shape discrimination in 7 organic liquid scintillation detectors is described. The system has been tested with a californium-252 source of dose rate 163 $\mu\text{Sv/hr}$ at 1 m and neutron emission rate of 1.5×10^7 per second into 4π and a maximum acquisition time of 2 hours, to characterize two $100 \times 100 \times 100$ mm concrete samples. The first of these was a solid sample and the second has a vertical, cylindrical void. The experimental data, supported by simulations with both Monte Carlo methods and MATLAB®, indicate that the presence of the internal cylindrical void, corners and inhomogeneities in the samples can be discerned. The potential for fast neutron assay of this type with the capability to probe hydrogenous features in large low-Z samples is discussed. Neutron tomography of bulk porous samples is achieved that combines effective penetration not possible with thermal neutrons in the absence of beam hardening.

Keywords: Tomography, fast neutrons, image reconstruction, scintillation detectors, voids.

1 Introduction

The interaction properties of neutrons with matter complement those of X-rays due to their lack of electrostatic interaction. Their scattering properties are largely independent of the atomic number of the elements that constitute the scattering medium whilst, conversely, they interact significantly with light (i.e. low-Z) isotopes particularly when thermalized. This is especially relevant for hydrogen (often as a constituent of water) and also for the other widespread elemental constituents of low-Z porous materials such as carbon, nitrogen and oxygen. These elements comprise a wide range of substances in use for structural applications and construction where non-destructive evaluation can be desirable. The application of neutron radiation is of interest as a complementary tool to X-ray computerized tomography (CT) because X-rays highlight high-Z features very effectively (such as the iron and cobalt in reinforcing bars and calcium in the surrounding cementitious matrix) whilst neutrons are effective for low-mass, low-density features such as porosity, hydration and fissures that attract low-mass deposits. Both neutron tomography (NT) and X-ray CT have a role in the non-destructive evaluation of the internal state and integrity of a wide variety of materials in use throughout the world.

The scientific prior art associated with NT over the last 30 years is very extensive. It has been applied to archaeological samples [1, 2], fossils and geological materials [3, 4, 5], as a probe for hydrogen content in turbine blades and metal casings [6, 7], as an assay for nuclear energy applications [8, 9, 10, 11, 12], to assess water evolution and flow in electrolyte fuel cells [13, 14], to assess the fouling of filter systems [15], the investigation of transport processes in biological matter [16, 17], the reverse engineering of metal components [18, 19], the imaging of

two-phase flow [20], the assessment of components used in fusion energy [21, 22] and in security applications for the detection and characterization of contraband [23, 24].

Neutron tomography systems usually comprise a source of neutrons, a collimator, a means for obtaining a variety of projections of a given sample (usually a rotating platform) and a detector system. Most applications have tended to source neutrons from a reactor [25, 26, 27], a spallation source [28, 29], linear accelerator [30] or portable neutron generator [31, 32, 33, 34]. Of particular relevance to the source used in this research is the use of the isotope californium-252 (^{252}Cf) in combination with plastic scintillators for time-tagged transmission radiography of residues in nuclear plant [35] and for the characterization and 2D imaging of materials [36]. For detectors most studies have used a scintillation screen (i.e. ^6Li -doped zinc sulphide or a plastic scintillator) coupled with a light intensification system; activation foils have also been used. Charge-coupled devices (CCDs) were first applied to NT approximately twenty years ago [37] and have been adopted widely due to their ease of use and compatibility with computerized data acquisition systems [38, 39, 40]. Recently, the use of plastic scintillators coupled to silicon photomultipliers with a portable D-D generator has been reported for NT [41] and a plastic scintillator (EJ-200) array with PMTs has been reported for induced fission radiography of nuclear materials [42].

By contrast, the use of organic scintillation detectors in NT, affording real-time pulse-shape discrimination (PSD) and thus the potential for combined acquisition of both neutron and γ -ray events, has not been explored extensively to date. However, organic scintillators with PSD (both plastics and liquids) have been used in neutron scatter cameras for the location and spectroscopy of isotopic neutron sources [43].

A further important distinction associated with extant methods of NT is the energy of the neutrons used. For the assessment of features in macroscopic samples cold or thermal neutrons have relatively low penetrating power limiting their use to thin samples. Several reports of the use of fast neutrons for radiography and tomography have been made [44, 45, 46, 47] which afford greater penetration desirable for bulk samples. However, their use requires different detection modalities with, for example, either organic scintillators or via prior moderation and then detection of the thermalized neutrons.

Relatively little research has been reported on the use of NT for the assessment of construction materials which forms part of the focus of this work and we are not aware of any reports of the use of fast neutrons for this purpose. Whilst NT has been used to investigate fluid transport in porous media [48, 49], in the context of its application to concrete described this paper two studies are prominent: Masschaele et al. [50] reported the use of thermal neutrons to study water ingress in small samples of autoclaved concrete and compared this with X-ray CT; Christie et al. [51] reported on the assessment of reinforced concrete in their comparison of thermal neutron tomography with X-ray CT. Of particular note is that they reported the limiting effect that scattering of thermal neutrons due to hydrogen content had on transmission. This resulted in a darkening and an associated lack of contrast towards the core of samples which was not observed in samples with low-water content such as sandstone and limestone. We reported recently [52] on the use of fast neutrons and a single liquid scintillation detector for the purposes of discerning rebar in concrete samples with a 75 MBq ^{252}Cf source. In this case the detector was shifted from position to position in turn and a general assessment of the relative abundance in terms of atomic number across the sample was inferred. There are a number of excellent

reviews summarizing both the NT field and the achievements of specific facilities around the world [53, 54, 55, 56].

The first objective of the research presented in this paper was to determine whether non-destructive NT could be achieved with PSD in organic liquid fast scintillators. We are not aware that this has been attempted before. Organic liquid scintillation detectors offer several advantages over existing detection methods for NT. For example, in comparison with two-stage light-conversion approaches based on CCDs, the light-to-electrical pulse conversion is confined within each detector unit obviating the need for downstream light-tight housings and mirror arrangements. In comparison with plastic scintillators (with the exception of EJ299) liquid scintillators exhibit PSD by which separate neutron- and γ -ray event streams can be derived. Real-time PSD [57] simplifies event processing across a detector array with both neutron and γ -ray data available at the point of each step of a scan rather than following extensive post-processing.

The second objective of this work was to explore the use of the liquid scintillation/PSD technique for the characterization of concrete to determine whether deep, macroscopic features such as a large void, could be discerned. Such features can be difficult to probe effectively with thermal neutrons. Whilst X-ray CT is recognized as a mature, high-resolution technique for concrete assay, the resolution of deep-seated features associated with hydration, porosity, water ingress along fissures etc. requires a combination of deep penetration and sensitivity to light isotopes that is not afforded by X-rays.

2 System description

The system described in this paper comprises:

- A relatively small isotopic neutron source,
- A collimator,
- A turntable offering vertical, rotational and horizontal displacement,
- Seven liquid detectors (Scionix, Netherlands) containing the EJ309 scintillant plus two in reserve (Eljen Technologies, TX),
- Two 4-channel MFAx4.3 analyzers (Hybrid Instruments Ltd, UK),
- An electronic counter interface,
- A PC running a dedicated acquisition/control graphical user interface (GUI) in LabVIEW® (National Instruments TX).

A CAD schematic of the complete system is shown in Fig. 1.

2.1 Source

For the purposes of this study a bare californium (^{252}Cf) source was used with a neutron emission rate of 1.5×10^7 per second into 4π , giving an associated neutron dose rate at 1 m of $163 \mu\text{Sv/hr}$ and an estimated γ -ray dose rate $8\text{-}10 \mu\text{Sv/hr}$ (not accounting for scatter). ^{252}Cf has two main decay pathways, one by α emission and one by spontaneous fission, the latter being the pathway of interest in this case as this is the principal source of fast neutrons.

The fact that the main process by which neutrons are emitted from ^{252}Cf is spontaneous fission is not of significance to this research because the coherence of the neutron emission in time has not been exploited. Rather, reliance has been placed on single-neutron counting. However, ^{252}Cf is one of the most widely-available, sealed, isotopic source materials for such measurements. It also has an energy spectrum sympathetic with this application (an average of

2.1 MeV and a most-probable energy of 0.7 MeV) in terms of transmission characteristics of the samples used. Further, the most likely energy of scattered neutrons in the environment that would act to degrade image quality, is below the energy cut-off of the scintillant (approximately 0.5 MeV) in the absence of a higher cut-off setting. Higher-energy sources (such as americium-beryllium) could be used with either their energy degraded by a hydrogenous substance or the implementation of a higher cut-off threshold to reduce the influence of the scattered component. The flux necessary for a suitable project to be achieved on a practical timescale was estimated using the Monte Carlo N particle (MCNP) code and the JANIS 4.0 display program, prior to design and construction of the system. A rubric was adopted such that the specified neutron flux needed to be sufficient to ensure a relative error of $< 5\%$ between unchanged projections.

2.2 Collimator

The use of the linear array of detectors adopted in this research required the use of a fan beam as opposed to a cone that might be used for example in established approaches with arrays of CCDs. This can have the disadvantage that more exposures or exposures of longer duration might be necessary but does have the benefit of reduced scatter from the surroundings since a fan beam is limited in how far it can stray above and below the target. This is especially relevant where the main source of reflection is a concrete floor or ceiling as is the case in most industrial environments.

The fan beam was formed using a collimator. The effective collimation of neutrons is not trivial given their tendency to reflect and be slowed down by light elements, and absorbed strongly by a few, specific isotopes that are usually low in abundance unless artificially enriched. In this research an arrangement was used in which two thick (relative to the width of the

collimating slot) slices of collimator material were combined into a stack to leave a thin, parallel aperture between them through which a horizontal fan of neutrons were able to pass.

The dimension of the collimator was matched to the optimum sample size under consideration in order to optimise the ratio of length-to-depth, minimise the object-to-detector distance and thus ensure a high spatial resolution in the tomographic results [58,59]. A variety of materials are suitable for use as a neutron collimator including water, high-density polyethylene, tungsten, iron and Perspex. MCNP simulations were performed to identify the best candidate and, whilst all performed satisfactorily, high-density polyethylene was selected as being relatively cheap & easy to machine and use. A collimator geometry of $500 \times 300 \times 360$ mm was selected, separated midway by a parallel aperture throughout of 3 mm. This was created by separating two 180 mm-thick polyethylene slabs with several spacers of equal thickness. As discussed with reference to the source earlier in this section, the degradation of the quality of the beam profile by scattering in a hydrogenous collimator is not expected to be as significant in this research as in other works because of the rapid fall in detector response of the organic scintillators for neutron energies < 500 keV which renders the detectors blind to the majority of scattered neutrons below this energy. This also simplifies the design of the collimator and removes the need for exotic thermal neutron absorber materials, such as gadolinium, bismuth and cadmium.

The collimator was modelled in MCNP5 [60] with a geometry corresponding to that specified in this research ($300 \times 360 \times 500$ mm) with a 3 mm central, horizontal slot. Neutrons reaching approximately 100% efficiency detector on the front face of the collimator were tracked to illustrate the geometry. These are shown in Fig. 2a. The beam profile in elevation, 1.5 m from the collimator, is shown in Fig. 2b. The source was located at (0,0,0) and the collimator

structure was located in the positive x-axis. The majority of these neutrons are shown to pass through the void slot in Fig. 2a with only a few passing through the collimator structure. The profile shown in Fig. 2b indicates the beam is fit for the intended purpose being approximately 1 cm wide at a range of 1.5 m from the collimator. The scalloping feature apparent in the profile is believed to be a result of the rectangular geometry of the polyethylene providing more collimation at the edges than in the middle.

2.3 Turntable

To rotate a sample in the horizontal plane and translate its position in the horizontal and vertical planes a turntable was manufactured. This was designed to minimize interference with the neutron field, and thus the majority of it is manufactured from aluminum. To be compatible with a variety of irradiation facilities the turntable was designed to be portable but sufficiently robust to withstand transport between sites, be rigid during operation and also to ensure the minimum of movement (slip and backlash) at each position. It was designed to provide a horizontal translation of 100 mm and a vertical translation of 110 mm to accommodate a maximum sample size of dimension 100 mm and a full 360° freedom of rotation.

Horizontal and vertical movements were each provided by lead screws actuated with a stepper motor (Igus, Germany); minimum step size of 0.0075 mm in the vertical, 0.02 mm per step in the horizontal. The rotational movement was provided by a timing belt and pulley mechanism giving a minimum angle of 0.27° per step consistent with a tolerance required for a quality image of at least 1°.

2.4 Detectors

Seven identical VS-1105-21 EJ309 scintillation detectors (Scionix, Netherlands) of cell dimension $100\text{ mm} \times 100\text{ mm} \times 120\text{ mm}$ were used. Each detector was placed in a vertical arrangement equidistant from the sample forming an arc as depicted in Fig. 1. This arrangement preserved the isotropy of the neutron flux according to its inverse-square dependence with distance. Thus in the absence of a sample that would otherwise perturb the flux each detector is positioned to return the same response irrespective of their position on the arc. Each detector has its own photomultiplier tube (PMT) of type 9821 FLB (ADIT Electron Tubes, Sweetwater, TX) and the high-voltage and anode signal cables were routed to the MFAX4.3 analyzers (Hybrid Instruments Ltd., UK). A total of nine detectors were placed in position (as shown in Fig. 1 and subsequently in Fig. 3) to enable swift substitution of up to two from the seven should any difficulties with detector stabilization arise during a scan.

Scattering from one detector to another constitutes a way in which a single neutron or γ ray can be misconstrued as two; in tomography this constitutes a potential source of noise on the image. To minimize this, measurements were made with a ^{137}Cs source and one detector in isolation and then with a second and a third at separations of 0 to 3 cm at 0.5 cm intervals. The influence of the additional detector(s) was observed to fall up to a spacing between them of 1 cm and hence this was the spacing used between detectors (any greater would undermine the system resolution and was also limited by the physical space available around the sample). The corresponding measurements for neutrons were not possible in the absence of an americium-beryllium source installed in place of the ^{252}Cf . However, it is worthy of note that the angle θ required for neutrons to scatter from detector to detector is relatively large, at $\theta \geq \pi/2$. Given the scattered neutron energy on hydrogen in laboratory frame varies as $E'_n = (1 + \cos \theta)E_n/2$

inter-detector scattering reduces the energy of the scattered neutrons significantly in an energy region where the sensitivity of the scintillant also falls rapidly.

2.5 Analyzers

The MFAX4.3 analyzers provide real-time pulse-shape discrimination (PSD) together with high-voltage control and PSD threshold setting. This enables events from each detector to be discriminated from γ rays in 333 ns with a jitter of 6 ns and an event throughput of 3×10^6 per second. Neutrons and γ rays are discriminated in real time as they are collected and separate signals corresponding to each are output from the analyzer in the form of 50 ns transistor-transistor logic (TTL) logic pulses [57]. PSD exploits the difference in long and short pulse shapes that arise for neutrons and γ rays, respectively [61] by comparing the heights of a sample of the pulse peak amplitude with another in the falling edge of the pulse after the pulses have been processed with a moving average filter [62]. For the purposes of this research only the neutron events were used. These were input directly into the NT counter system; a separate input was provided for each of the seven detectors.

2.6 Counter interface, control circuitry and graphical user interface

The control system governing the tomography acquisition process carries out the following functions:

- To interpret a LabVIEW® [63] command file governing the start/end points and the size of the translational/rotational increment as set by the user,

- Convert this to a control signal to actuate the turntable to the required sequence of positions in turn,
- When rested in position, count the neutron events for a specified period of time,
- At the end of that period stop the count and move to the next position,
- Finally, format the count data consistent with the requirements of a separate analysis PC to ensure compatibility with the reconstruction process that is performed after data acquisition.

The counter module of the interface circuitry counts each 50 ns TTL pulse signal from each neutron produced by the MFAx4.3 analyzers at high frequency (maximum 3 MHz). This has been designed to afford a capacity of 64 counting channels (32 neutron and γ -ray signals) to cater for the total number of detectors currently available at Lancaster for expansion in the future. A 32-bit counter was designed and constructed to allow for long-duration assessments and the large numbers of counts that would arise.

An open-loop control mode was selected for the purposes of simplicity in the first instance, with three DC stepper motors selected to drive the pulley system and each of the lead screws. Commercially-available stepper motor drive circuits (Quasar Electronics) were used, actuated by a microcontroller (Arduino.cc). The microcontroller served to interpret the user-configured settings from the LabVIEW® command file and hence to provide the corresponding signal stimulus to the control motor circuits to carry out the required operations needed to place the sample into the next required position. Once stationary, a microcontroller in the counter circuitry records the number of neutron events, stops the count and transfers the count data to the LabVIEW® interface ready for reconstruction. It then moves the turntable to the next position before beginning to count again.

2.7 Image reconstruction

Reconstruction was performed offline in MATLAB ® [64]. Preliminary investigations of candidate reconstruction methodologies showed that a traditional Filtered Back-Projection approach would result in unsatisfactory image quality. This was due to the relatively large sensitive volume of the detectors used and the need for a finite degree of spacing between the detectors in order to reduce the extent of inter-detector scattering discussed earlier. Due to the large volume of the detectors, the beam window for each detector penetrated a large proportion of the sample space resulting in a low spatial resolution of the sample features. The spaces between the detectors resulted in transient areas where attenuation data were not present and thus required interpolation.

An alternative imaging approach was thus developed with the aim of varying the beam coverage of the sample in order to maximize the spatial resolution of the final image. The use of a sinograph, as in Filtered Back-Projection and methodologies such as ART, was found to be restrictive in forcing the image to be described from one rotational viewpoint. Therefore the new methodology sought to account for arbitrary beam sizes and orientations by applying detector readings from each projection directly into corresponding image matrix pixels. To use this new spatial freedom to good effect, the sample was moved incrementally across a path perpendicular to the neutron beam at each rotational stage, scanning the large beam window of the detectors across the sample and thus providing further attenuation data localized in volumes of the sample newly illuminated by each incremental movement.

The reconstruction script calculated the beam coverage over the sample for each projection and mapped this in order to determine the pixels to be adjusted. The coverage data were then

used to determine and account for the amount of readings collected for each pixel. The script was adapted to make use of simulation both through idealized artificial data and through the use of MCNPX, thus allowing testing and optimization of the process.

This approach provided superior results to those achievable with existing methods and produced images of good spatial resolution from the relatively large detectors used in this research. The process demonstrated reasonable definition for corners, voids within samples and volumes with lower neutron attenuation coefficients but there are some small artefacts thought to be produced as a result of the transient areas between detectors. Low-pass filtering was used to reduce the significance of these artefacts but aggressive cut-off filtering was found to reduce spatial resolution.

3 Modelling and simulations

Two approaches to modelling the performance of the system have been adopted in this work: i) a deterministic approach with MATLAB[®] and ii) a stochastic transport simulation using Monte Carlo methods. The results from these approaches are combined for comparison with the experimental results in Section 5.

3.1 MATLAB[®] simulations

Performing MCNP simulations for each increment in each of the degrees of freedom would have been impractical for every feasible scenario during the development of the system design so instead an idealized reconstruction was carried out. This used the established MATLAB[®] script for the reconstruction process together with an analytical approximation of the attenuation of a given sample on the response of a detector. This approximation replaced a stochastic description

of the detector response with an array of pixels in space. This array represents the effect the object would have on the neutron flux according the Beer-Lambert law of attenuation.

3.2 Monte Carlo N Particle code methods

The geometrical set-up of the system was constructed in MCNP5 [60] within the dimensional constraints of the environment in which the experimental measurements were made i.e. concrete floor etc. The objective of the MCNP simulations was to clarify the feasibility of the measurement in terms of specifying the number of detectors, optimum arrangement and the size of the collimator aperture. The source was modelled as a point, isotropic ^{252}Cf with a Watt fission spectrum across 99 bins from 0 to 20 MeV with no energy cut-off. The simulation included features corresponding to the collimator, the sample, the turntable and the detectors running 1 million particles in neutron mode. Nine of the scintillation detectors were included as aluminium blocks that matched the approximate dimensions of the $100 \times 100 \times 100$ mm EJ-309 scintillators in order to infer how many neutrons would be incident on the front face of each detector. This approach omitted the neutron interactions with any of the other surfaces and the scintillant itself in order to minimise the effects of scatter. Only the heads of the scintillators were modelled i.e. without the PMTs and stands. In order to measure the values obtained for the readings the average surface flux tally was selected. This allowed individual readings from each of the front faces of the detectors to be taken in terms of neutron flux. This could then be interpreted in the same way as the practical measurements and reconstructed to give corresponding and comparable images.

The MCNP simulations were limited relative to the experimental set-up because the scintillant was not included in the detector configuration. No account was made of the scattering between detectors notwithstanding the measures described in Section 2.4.

4 Experimental methods

The experiments described in this paper were performed at the National Physical Laboratory (NPL), Teddington, UK. The source used was a bare i.e. unmoderated ^{252}Cf as described earlier in Section 2. The tomography system was set up as described above and as shown in-situ at NPL in Fig. 3. Singles neutron events were fed to the analysis instrumentation, synchronized automatically with the capture of data at each position of the sample under study to constitute a given projection.

The sample under test was mounted on the rotary table to move it throughout 360° in the plane parallel with the floor and, simultaneously, over a user-specified number of positions in the horizontal plane. The number of increments and the duration at each increment was configured on a case-by-case basis where necessary to optimize the quality of the recovered tomograph as summarized below in Table 1. The vertical translation was not explored in these experiments.

Two samples were prepared for focus of this study, both of concrete. The first was a solid, square cube and the second is a cube with a steel, hollow pipe through the center located with the pipe in the vertical plane. The pipe-based sample is shown in Fig. 4, along with its CAD representation. Both samples were mixed with a vibrator to ensure uniform composition and formed with a mold in each case. The proportions used were identical in each case corresponding to 3 parts aggregate, 2 parts sand and 1 part cement. The curing of the samples was prolonged by covering each sample with a polythene sheet to encourage uniform porosity and to prevent crackling and crumbling at the edges. The dimension of the samples was $100\times 100\times 100$ mm and the pipe insert was 100 mm in length with a diameter of 50 mm. The choice of samples was made to determine whether the discontinuities associated with the corners

of a cuboid sample could be discerned from a form with cylindrical symmetry, and whether the system was able to differentiate between a solid sample and one with a hollow, steel-lined cylindrical void as discussed in Section 1. For the purpose of comparison the composition of the samples used in the MCNP simulations was selected as Hanford dry concrete [65] with a density of 2.18 g cm^{-3} and an atomic density of $0.0664 \text{ atoms b}^{-1} \text{ cm}^{-1}$.

In order to ensure the high-voltage settings are uniform across the detector array, a radioactive caesium source (^{137}Cs) was used to calibrate them. Caesium is chosen because of its ^{137}Cs decay via β emission to the metastable isomer $^{137\text{m}}\text{Ba}$; which decays subsequently with the emission of a single $662 \text{ keV } \gamma$ ray. This monoenergetic line enables the response of each detector to be standardized against one another in terms of the position of the corresponding Compton edge in each pulse-height spectrum. This was achieved by adjusting the high-voltage supply level to each PMT until the positions are the same across the array. Then the low-energy thresholds for each detector were adjusted to be consistent with one another and the PSD threshold for each detector was fixed in correspondence with the neutron- γ -ray event data [57]. Once this was completed each sample could be tested in turn for a variety of translational and rotational steps as indicated in the following results. A summary of the duration, type and extent of the increments used in the measurements is given in Table 1.

Table 1: A summary of the experimental measurements made in terms of the sample type, duration of increments, number, step and type of increment.

Analysis		Duration of increment / s	Number of increments	
			Rotational	Horizontal
Solid sample	Figure 5a	12	16 @ 22.5°	20 @ 3.08 mm
	Figure 5b	12	12 @ 30.0°	15 @ 4.10 mm
Void sample	Figure 6	16	17 @ 21.2°	26 @ 2.30 mm

5 Results

In Fig. 5a the fast neutron tomograph obtained for the solid concrete sample is shown for measurements performed over an hour's duration comprising 16 rotational increments and 20 horizontal translations. In Fig. 5b the corresponding tomograph is given for the sample with the central void formed by the steel pipe insert, based on 12 rotations and 15 translations.

In Fig. 6, the same voided sample has been scanned for 2 hours comprising 17 rotations and 26 translations. Figs. 5a, 5b and 6 also include overlays to illustrate the actual dimension of the sample in each case. In Figs. 7a and 7b the results arising from simulations with MATLAB® and MCNP are provided for comparison with the tomographs from Figs 5a and 5b, reproduced in monochrome and on the same scales.

6 Discussion

The confirmation that image quality increases with the number of translations (evidenced by the qualitative comparison of Fig. 5b with Fig. 6) is a potential advantage for applications of the technique. Alternative approaches to increase tomographic resolution include either increasing the neutron flux or increasing the number of detectors. However, assuming the flux cannot be increased by further optimization of the geometry a source of greater activity might be inconvenient in terms of regulatory control whereas increasing number of detectors might render the system less portable and more expensive.

A quantitative assessment of the spatial resolution has been made on the basis of the 10%-90% edge transition distance and this is given in Table 2 for the solid/void samples and for the short/long duration experimental measurements and the MCNP and MATLAB® simulations. It

is evident that whilst the void sample tomograph is clearer to the eye this is not reflected in the spatial resolution analysis within the uncertainty of ± 1 mm.

Table 2: Estimations of the spatial resolution based on the 10%-90% edge response of the experimental, MCNP and MATLAB[®] analyses for the solid and void concrete samples. The uncertainty in the resolutions is estimated as ± 1 mm.

Spatial resolution analysis		Experimental		MCNP	MATLAB [®]
		Short	Long		
Edge response / 10%-	Solid sample	10	-	10	7
90% range / mm	Void sample	10	10	7	5

There are some distinctions between the simulation results and the experimental data which could be due to a number of inconsistencies between the input data to the simulations & the real system and its operation. These might include, for example: artefacts arising from the reconstruction process; beam hardening [66] (an upwards shift in the average energy of the neutron flux as its lower-energy component is reduced due to being scattered out of the sample or absorbed within it); variance in the geometry of the sample position and subsequent scaling of transformations or changes in the system set-up (particularly drifts in the high-voltage supplies to the PMTs). In particular, the differences in the alignment and positioning that are evident from a comparison of Figures 5b and 6 are consistent with limitations in the accuracy of the positioning control system whilst stabilized digital HV supplies are used and thus significant drift in the

PMTs is not considered significant. With regards to the potential for beam hardening two neutron spectra produced with MCNP are shown in Figures 8a and 8b, before and after the concrete sample respectively. The average neutron energy calculated with these data before the sample is 1.79 MeV and afterwards 2.26 MeV illustrating that beam hardening by the sample does occur. For concrete the corresponding reduction in total macroscopic cross-section is approximately 25% with the most significant contributions being from the hydrogen, oxygen and aluminum in the sample.

In the future it would be interesting to compare the response with an americium-beryllium source in place of californium-252 to investigate the effect of the higher-energy spectrum of the former on the quality of the images. Also, the system could be optimized beyond the arrangement described in this work via, for example, increasing the number of detectors (thus raising the overall detection efficiency), reducing the volume of the detectors to increase the image resolution which would also enable narrower gaps between the detectors combined with hydrogenous shielding to reduce the effect of scatter between detectors. Further increases in resolution might be achieved by integrating a more sophisticated method of closed-loop control, as opposed to the open-loop control approach used in this research, with which to increase the accuracy of the position setting. A more detailed study of the uncertainties in the response of the system in correspondence with the simulations would enable these to be discerned more effectively from the competing influence of properties of the samples; the latter might include localized variations in density, water of crystallization, hydration and beam hardening. This would enhance our understanding of sensitivity of the system to revealing these physical characteristics.

7 Conclusions

The conclusions from this research are as follows:

- The experimental data presented in this paper demonstrate that fast neutron tomography with real-time PSD and a relatively small number of organic scintillation detectors is feasible [67].
- Useful tomographic data are obtained in less than two hours that enable solid and voided concrete samples to be discerned from one another.
- The physical size of the samples and their features (corners, the cylindrical void etc.) are observed to correlate consistently with the true dimensions of these features.
- Where the number of translations has been increased image quality is improved evident as a result of the refinement of the pitch of the translational increments of the measurements with relatively little increase in acquisition time.
- Both qualitative and quantitative agreement is observed between the results of the MATLAB ® simulations, those arising from MCNP calculations and the experimental data with an experimental spatial resolution based on the 10%-90% edge resolution of (10 ± 1) mm.
- The technique demonstrates that penetration is effective in resolving the void whilst simultaneously depicting those areas of high absorption/scattering adjacent to it. This is in contrast with earlier reports [51] on the use of thermal neutrons on concrete where penetration was too limited to reveal detail beyond the outer surface of concrete samples.

Acknowledgment

We acknowledge Dr Neil Roberts at NPL for the provision of the ^{252}Cf source, Mark Salisbury for the manufacture of the concrete samples and Alex Grievson for the beam hardening calculations. This research was funded in part by Lancaster University, UK, and also via the Engineering and Physical Sciences Research Council (EPSRC) as part of the National Nuclear User Facility (www.nnuf.ac.uk), grant number EP/L025671/1.

References

- [1] Schulze R., Szentmiklosi L., Kudejova P., Canella L., Kis Z., Belgia T., Jolie J., Ebert M., Materna T., Biro K.T., Hajnal Z., The ANCIENT CHARM project at FRM II: Three-dimensional elemental mapping by prompt gamma activation imaging and neutron tomography, (2013) *Journal of Analytical Atomic Spectrometry*, 28 (9), pp. 1508-1512.
- [2] Pereira M.A.S., Schoueri R., Domienikan C., Toledo F.D., Andrade M.L.G., Pugliesi R., The neutron tomography facility of IPEN-CNEN/SP and its potential to investigate ceramic objects from the Brazilian cultural heritage, (2013) *Applied Radiation and Isotopes*, 75, pp. 6-10.
- [3] Martins R.M.S., Beckmann F., Castanhinha R., Mateus O., Pranzas P.K. Dinosaur and crocodile fossils from the mesozoic of Portugal: Neutron tomography and synchrotron-radiation based micro-computed tomography, (2011) *Materials Research Society Symposium Proceedings*, 1319, pp. 319-332.
- [4] Koliiji A., Carminati A., Kaestner A., Vulliet L., Laloui L., Fluehler H., Vontobel P., Hassanein R., Experimental Study of Flow and Deformation in Aggregated Soils using Neutron Tomography, (2010) *Advances in X-ray Tomography for Geomaterials*, pp. 341-348.

- [5] Vontobel, P., Lehmann, E. and Carlson, W. D., Comparison of x-ray and neutron tomography investigations of geological materials, (2005) IEEE Transactions on Nuclear Science, vol. 52 (1), pp. 338-341.
- [6] Sim, C. M., Oh, S. H., Kim, T. J., Lee, Y. S., Kim, Y. K., Kwak, S. S. and Hwang, Y. H., Detecting internal hot corrosion of in-service turbine blades using neutron tomography with Gd tagging, J. Nondestructive Evaluation 33 (4) pp. 493-503 (2014).
- [7] Gibbons M.R., Richards W.J., Shields K., Optimization of neutron tomography for rapid hydrogen concentration inspection of metal castings, (1999) Nuclear Instruments and Methods in Physics Research, Section A: Accelerators, Spectrometers, Detectors and Associated Equipment, 424 (1), pp. 53-57.
- [8] Zboray R., Prasser H.-M., Optimizing the performance of cold-neutron tomography for investigating annular flows and functional spacers in fuel rod bundles, (2013) Nuclear Engineering and Design, vol. 260, pp. 188-203.
- [9] Agrawal A., Kashyap Y., Sarkar P.S., Behra A.N., Shukla M., Singh R.N., Sinha A., Chakravartty J.K., Study of hydride blisters in Zr-alloy using neutron tomography, (2012) Journal of Nuclear Materials, 421 (1-3), pp. 47-53.
- [10] Kickhofel J.L., Zboray R., Damsohn M., Kaestner A., Lehmann E.H., Prasser H.-M., Cold neutron tomography of annular coolant flow in a double subchannel model of a boiling water reactor, (2011) Nuclear Instruments and Methods in Physics Research, Section A: Accelerators, Spectrometers, Detectors and Associated Equipment, 651 (1), pp. 297-304.
- [11] Richards W. J., McClellan G. C., Tow D. M., Neutron tomography of nuclear fuel bundles, (1982) Mater. Eval, V 40 (N 12), pp. 1263-1267.

- [12] Betten P. R., Tow D. M., LMFBR fuel bundle distortion characterization using neutron tomography and potting, (1984) *Materials Evaluation*, (6), pp. 815-821.
- [13] Coakley, K. J., Vecchia, D. F., Hussey, D. S., Jacobson, D. L., Neutron tomography of a fuel cell: Statistical learning implementation of a penalized likelihood method, (2013) *IEEE Transactions on Nuclear Science*, 60 (5), art. no. 6616604, pp. 3945-3954.
- [14] Santamaria A., Tang H.-Y., Park J.W., Park G.-G., Sohn Y.-J., 3D neutron tomography of a polymer electrolyte membrane fuel cell under sub-zero conditions, (2012) *International Journal of Hydrogen Energy*, 37 (14), pp. 10836-10843.
- [15] Toops T.J., Bilheux H.Z., Voisin S., Gregor J., Walker L., Strzelec A., Finney C.E.A., Pihl J.A., Neutron tomography of particulate filters: A non-destructive investigation tool for applied and industrial research, *Nuclear Instruments and Methods in Physics Research, Section A: Accelerators, Spectrometers, Detectors and Associated Equipment*, 729, pp. 581-588 (2013).
- [16] Aregawi W., Defraeye T., Saneinejad S., Vontobel P., Lehmann E., Carmeliet J., Derome D., Verboven P., Nicolai B., Dehydration of apple tissue: Intercomparison of neutron tomography with numerical modelling, (2013) *International Journal of Heat and Mass Transfer*, 67, pp. 173-182.
- [17] Alghamdi A.A., Monte Carlo simulation of neutron tomography for palm weevil detection, (2012) *Journal of Radioanalytical and Nuclear Chemistry*, 291 (2), pp. 359-364.
- [18] Roos T.H., Quin R.L., De Beer F.C., Nshimirimana R.M., Neutron tomography as a reverse engineering method applied to the IS-60 Rover gas turbine, (2011) *Nuclear Instruments and Methods in Physics Research, Section A: Accelerators, Spectrometers, Detectors and Associated Equipment*, 651 (1), pp. 329-335.

- [19] Schillinger B., Blumhuber W., Fent A., Marcus Wegner, 3D neutron tomography: Recent developments and first steps towards reverse engineering, (1999) Nuclear Instruments and Methods in Physics Research, Section A: Accelerators, Spectrometers, Detectors and Associated Equipment, 424 (1), pp. 58-65.
- [20] Hussein E.M.A., Meneley D.A., Banerjee S., Single-exposure neutron tomography of two-phase flow, (1986) International Journal of Multiphase Flow, 12 (1), pp. 1-34.
- [21] Greuner H., Schillinger B., Linsmeier Ch., Neutron tomography as a new method for the three-dimensional structure analysis of CFC as plasma-facing material, (2011) Physica Scripta T, T145, art. no. 014074,
- [22] Khovanskii A.V., Skopintsev D.A., Kuz'mina S.A., Application of the trial-and-error method for solving the inverse radon problem for ITER neutron tomography, (2006) Instruments and Experimental Techniques, 49 (2), pp. 203-206.
- [23] Da Silva A.X., Crispim V.R., Neutron tomography using projection data obtained by Monte Carlo simulation for nondestructive evaluation, (2002) Revista Brasileira de Ciencias Mecanicas/Journal of the Brazilian Society of Mechanical Sciences, 24 (4), pp. 309-311.
- [24] Miller T. G., Use of neutron tomography for airline security, (1994) Proceedings of SPIE - The International Society for Optical Engineering, 2093, pp. 204-217.
- [25] R. M. Schoueri, C. Domienikan, F. de Toledo, M. L. G. Andrade, M. A. Stanojev Pereira and R. Pugliesi, The new facility for neutron tomography of IPEN-CNEN/SP and its potential to investigate hydrogenous substances, (2014) App. Rad. Isot. vol. 84, pp. 22-26.
- [26] Pereira M.A.S., Marques J.G., Pugliesi R., A Simple Setup for Neutron Tomography at the Portuguese Nuclear Research Reactor, (2012) Brazilian Journal of Physics, 42 (5-6), pp. 360-364.

[27] Kureta M., Development of an ultra-high-speed scanning neutron tomography system for high-quality and four dimensional visualizations, Nucl. Inst. Meth. Phys. Res. A 605 (2009) 81-84.

[28] Burca G., James J.A., Kockelmann W., Fitzpatrick M.E., Zhang S.Y., Hovind J., Van Langh R., A new bridge technique for neutron tomography and diffraction measurements, (2011) Nuclear Instruments and Methods in Physics Research, Section A: Accelerators, Spectrometers, Detectors and Associated Equipment, 651 (1), pp. 229-235.

[29] Kamiyama T., Tsukui D., Sato H., Kiyonagi Y., Accelerator-based neutron tomography cooperating with X-ray radiography, (2011) Nuclear Instruments and Methods in Physics Research, Section A: Accelerators, Spectrometers, Detectors and Associated Equipment, 651 (1), pp. 28-31.

[30] Tang, V. Rusnak, B. Falabella, S. Hawkins, S. McCarrick, J. F., Wang, H., Hall, J. M. and Ellsworth, J., Accelerator driven gamma and fast neutron radiography test-bed at Lawrence Livermore National Laboratory, (2013) AIP Conf. Proc. 1525, pp. 714-719.

[31] Andersson, P. Andersson-Sunden, E. Sjöstrand, H. and Jacobsson-Svard, S., Neutron tomography of axially-symmetric objects using 14 MeV neutrons from a portable generator, (2014) Review of Scientific Instruments vol. 85 (8) art. No. 085109.

[32] Fantidis, J. G., Fast and thermal neutron radiographies based on a compact neutron generator, (2012) Journal of Theoretical Applied Physics, vol. 6 (20) pp. 1-8.

[33] Fantidis, J. G., Nicolaou, G. E. and Tsagas, N. F., Optimisation study of a transportable neutron radiography unit based on a compact neutron generator, (2010) Nucl. Inst. Meth. Phys. Res. A618 , pp. 331-335.

- [34] Andersson, P. Valldor-Blücher, J. Andersson Sundén, E. Sjöstrand H. and Jacobsson-Svärd, S. Design and initial 1D radiography tests of the FANTOM mobile fast-neutron radiography and tomography system, (2014) Nucl. Inst. Meth. Phys. Res. A756, pp. 82-93.
- [35] Uckan, T., Wyatt, M. S., Mihalczo, J. T., Valentine, T. E., Mullens, J. A. and Hannon, T. F., Fissile deposit characterization at the former Oak Ridge K-25 gaseous diffusion plant by ^{252}Cf -source-driven measurements, ORNL/TM-13642 (1998).
- [36] Stevanato, L. Caldugno M. Dima, R. Fabris, D. Hao, X. Lunardon, M. Moretto, S. Nebbia, G. Pesente, S. Pino, F. Sajo-Bohus, L. and Viesti, G., A new facility for non-destructive assay using a ^{252}Cf source, (2013) Applied Radiation and Isotopes, vol. 73, pp. 52-59.
- [37] Pfister G., Maier P., Hehn G., Kегreiss W., Stier G., Neutron Tomography for Non-Destructive Material Testing, (1985) Atomkernenergie, Kerntechnik, vol. 47 (4), pp. 242-245.
- [38] Richards W.J., Gibbons M.R., Shields K.C., Neutron tomography developments and applications, (2004) Applied Radiation and Isotopes, vol. 61 (4), pp. 551-559.
- [39] Vontobel P., Lehmann E. H., Hassanein R. and Frei G., Neutron tomography: method and applications, (2006) Physica B: Condensed Matter vol. 385-386 (1) 475-480
- [40] Sinha A., Shaikh A.M., Shyam A., Development and characterization of a neutron tomography system based on image intensifier/CCD system, (1998) Nuclear Instruments and Methods in Physics Research, Section B: Beam Interactions with Materials and Atoms, vol. 142 (3), pp. 425-431.
- [41] Adams R., Zboray R., Prasser H. –M.. A novel fast-neutron tomography system based on a plastic scintillator array and a compact D-D neutron generator, (2016) Applied Radiation and Isotopes, vol. 107, pp. 1-7.

- [42] Mullens, J. McConchie, S. Hausladen, P. Mihalcz, J. Grogan, B. Sword, E. (2011) Neutron radiography and fission mapping measurements of nuclear materials with varying composition and shielding, Proc. Institute of Nuclear Materials Management, Desert Palm, CA, July 17-21.
- [43] Brennan, J, Brubaker, E, Cooper, R, Gerling, M, Greenberg, C, Marleau, P; Mascarenhas, N and Mrowka, S, Measurement of the Fast Neutron Energy Spectrum of an Am-241-Be Source Using a Neutron Scatter Camera, (2011) IEEE Transactions on Nuclear Science. vol. 58 (5), pp. 2426-2430
- [44] Kamiyama T., Miyamoto N., Tomioka S., Kozaki T., Quantitative epithermal neutron tomography with compact pulsed neutron source, (2009) IEEE Nuclear Science Symposium Conference Record, art. no. 5402369, pp. 1266-1270.
- [45] Bücherl, T., von Gostomski, Ch. Lierse, Breitzkreutz, H., Jungwirth, M. and Wagner, F. M., NECTAR—A fission neutron radiography and tomography facility, (2011) Nucl. Inst. Meth. A651 pp. 86-89).
- [46] Lee, S. Rinchel, T. Doskow J. and Sokol, P. E. Three-dimensional (3D) fast neutron tomography at the low energy neutron source (LENS), (2014) Phys. Proc. vol. 60, pp. 118-124.
- [47] Rusnak, B. Hall, J.M. Fitsos, P. Souza, R. Jong, M., A large-format imaging optics system for fast neutron radiography, (2007) Proc. IEEE Part. Acc. Conf. 4440657 pp. 3029-3031.
- [48] Gilbert A.J., Deinert M.R., Neutron tomography of axisymmetric flow fields in porous media, (2013) Nuclear Instruments and Methods in Physics Research, Section B: Beam Interactions with Materials and Atoms, vol. 301, pp. 23-28.
- [49] Schaap J.D., Lehmann P., Kaestner A., Vontobel P., Hassanein R., Frei G., de Rooij G.H., Lehmann E., Fluhler H., Measuring the effect of structural connectivity on the water dynamics in

heterogeneous porous media using speedy neutron tomography, (2008) *Advances in Water Resources*, vol. 31 (9), pp. 1233-1241.

[50] Masschaele, B., Dierick, M., Cnudde, V., Van Hoorebeke, L., Delputte, S., Gildemeister, A., Gaehler, R. and Hillenbach, A., High-speed thermal neutron tomography for the visualization of water repellents, consolidants and water uptake in sand and lime stones, (2004) *Rad. Phys. Chem.* vol. 71, pp. 807-808.

[51] Christe, P., Bernasconi, M., Vontobel, P., Turberg, P. and Parriaux, A., Three-dimensional petrographical investigations on borehole rock samples: a comparison between X-ray computed- and neutron tomography, (2007) *Acta Geotechnica*, vol. 2, pp. 269-279.

[52] K. Mitton, A. Jones and M. J. Joyce, Digital fast neutron radiography of steel reinforcing bar in concrete, (2014) *Journal of Instrumentation*, vol. 9 C12045.

[53] Sinha A., Sarkar P.S., Kashyap Y., Roy T., Agrawal A., Development and applications of X-ray and neutron tomography for nuclear and industrial applications, (2008) *AIP Conference Proceedings*, 1050, pp. 45-56.

[54] Kardjilov N., *Neutron Phase-Contrast and Polarized Neutron Tomography*, (2008) in: *Advanced Tomographic Methods in Materials Research and Engineering*, ed. Banhart, J., Oxford Scholarship Online, ISBN-13: 9780199213245.

[55] Winkler B., Applications of neutron radiography and neutron tomography, (2006) *Reviews in Mineralogy and Geochemistry*, vol. 63, pp. 459-471.

[56] Vontobel P., Lehmann E.H., Hassanein R., Frei G., *Neutron tomography: Method and applications*, (2006) *Physica B: Condensed Matter*, vol. 385-386 I, pp. 475-480.

- [57] Joyce, M.J. Gamage, K.A.A. Aspinall, M.D. Cave, F.D. Laviertes, A., Fast Neutron Coincidence Assay of Plutonium with a 4-Channel Multiplexed Analyzer and Organic Scintillators, (2014) IEEE Transactions on Nuclear. Science, vol. 61 (3) pt. 2 pp. 1340-1348.
- [58] B. Schillinger, B. Lehmann, E. and Vontobel, P. (2000) 3D neutron computed tomography: requirements and applications, Physica B, pp. 59-62.
- [59] M. Radebe, M. Beer, F. Kaestner, A. Lehmann, E. Sim, C. and Sideras-Hadded, E. (2013) Evaluation procedures for spatial resolution and contest standards for neutron tomography, Procedia, vol. 43, pp. 138-148.
- [60] <https://mcnp.lanl.gov/>
- [61] Brooks, F. D., A scintillation counter with neutron and gamma-ray discriminators, (1959) Nuclear Instruments and Methods, vol. 4 (3) pp. 151-163.
- [62] D'Mellow, B. Aspinall, M. Mackin R. and Joyce, M. J., Digital n- γ discrimination in liquid scintillators using pulse gradient analysis, (2007) Nuclear Instruments and Methods vol. A578 (1) pp. 191-197.
- [63] Elliott, C. Vijayakumar, V. Zink, W. Hansen, R., National Instruments LabVIEW: A programming environment for laboratory automation and measurement, (2007) Journal of the Association for Laboratory Automation, vol. 12 (1) , pp. 17-24.
- [64] <http://uk.mathworks.com/>
- [65] McConn Jr, R. J. Gesh, C. J. Pagh, R. T. Rucker, R. A. Williams III, R. G., (2011) Compendium of material composition data for radiation transport modelling, PNNL-15870 Rev. 1.
- [66] Dawson, M. N., (2008), Applications of neutron radiography and tomography, PhD thesis, University of Leeds, UK.

[67] Patent application, 27 July 2015, 'Method of tomography', GB1513188.1

Fig. 1. A CAD representation of the tomography system set-up, showing 9 detectors (right), turntable and sample (center-left) & collimator (left).

Fig. 2. a) MCNP5 [60] simulations of 10^5 neutron tracks from ^{252}Cf through the polyethylene collimator structure used in this research, side elevation (left) and plan view (right). b) The beam profile in elevation simulated with MCNP5 [60], 1.5 m from the collimator as a function of height depicted on the left (relative to 0 corresponding to the position of the slot) and relative neutron flux as per the scale on the right.

Fig. 3. The system at NPL: Polyethylene collimator (background, left), rotary table and sample (mid-ground, left), detectors (foreground, right). The analyzers are not in view in this photograph.

Fig. 4. Concrete sample with a vertical cylindrical void formed by a steel tube insert (left) and the corresponding truncated CAD schematic (right).

Fig. 5. a) A fast neutron tomograph for the solid concrete cube sample based on an acquisition over 16 rotations and 20 translations. b) A tomograph of the concrete sample with steel pipe through its centre based on acquisition over 12 rotations and 15 translations. Total run time 1 hour for each sample and each tomograph is shown with an overlay of the true dimension of the sample and of the central void. Intensity key: blue = high transmission (low density), green-yellow = intermediate transmission, red-black=low transmission.

Fig. 6. A fast neutron tomograph for the concrete sample with steel pipe through the center based on acquisition over 17 rotations and 26 translations, total run time 2 hours, shown with an overlay of the true dimension of the sample and the void. Intensity key is as for Fig. 5.

Fig. 7. a) Fast neutron tomographs for the solid concrete cube sample for 16 rotations, 20 translations and b) for the concrete cube sample with steel pipe through its centre, 17 rotations, 26 translations. MATLAB ® simulations (left), MCNP simulations (center) and experimental results (right).

Fig. 8. MCNP simulation results of neutron spectra arising from a ^{252}Cf Watt spectrum with 10^{10} neutrons incident on the polyethylene collimator to illustrate the effect of beam hardening a) after the collimator but before the concrete sample with an average neutron energy 1.79 MeV and b) after the concrete sample with an average neutron energy 2.26 MeV.

Fig. 1

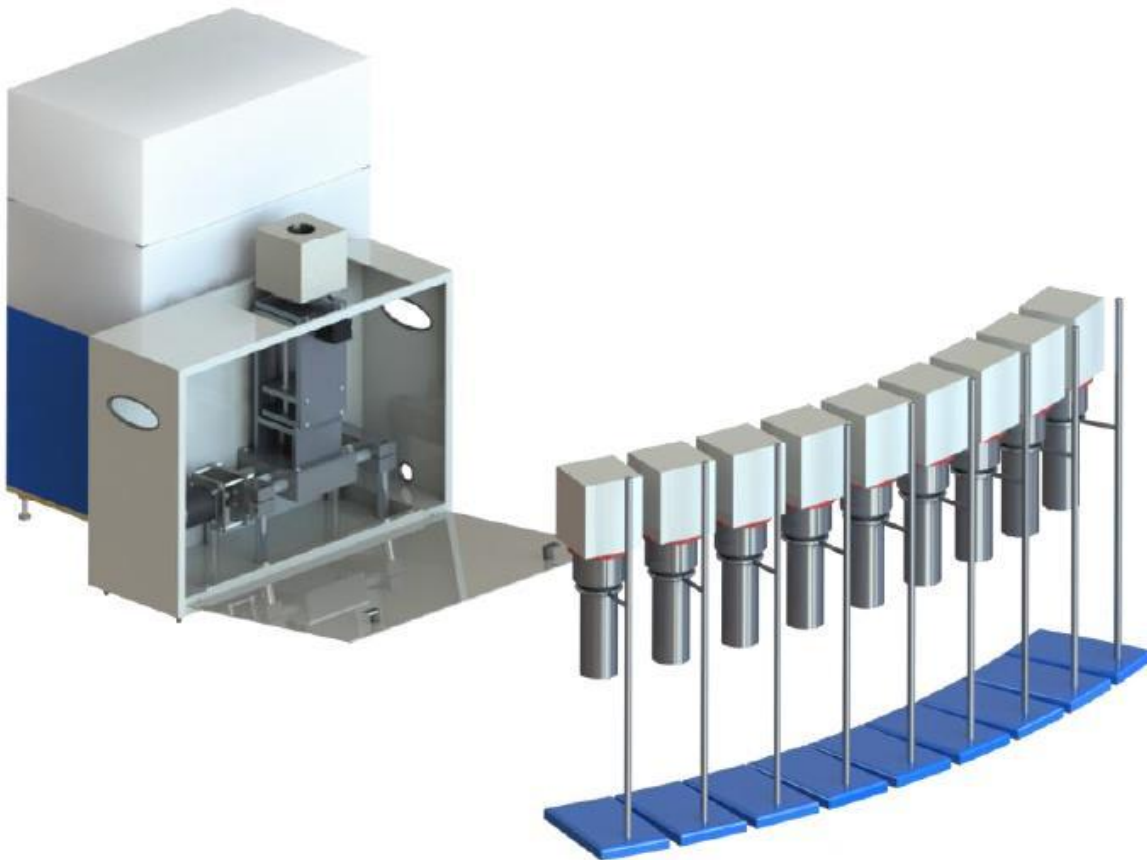


Fig. 2a

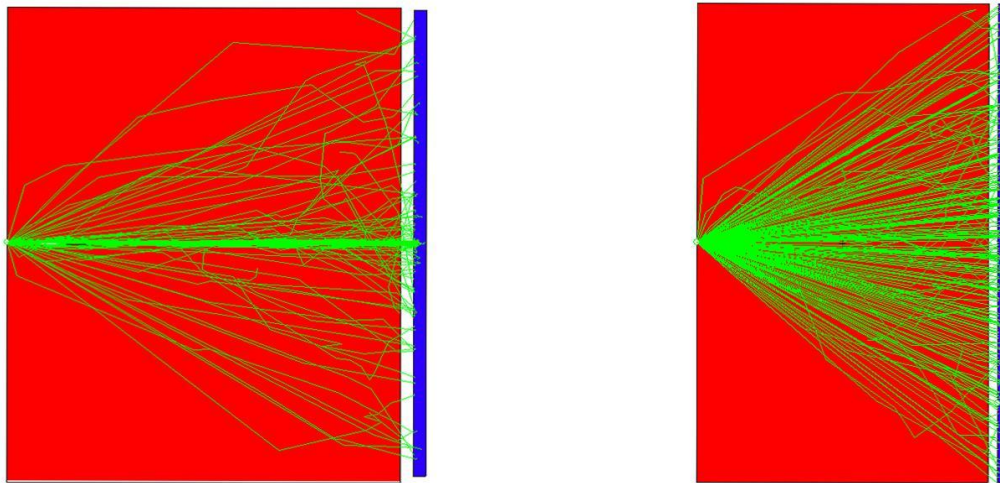


Fig. 2b

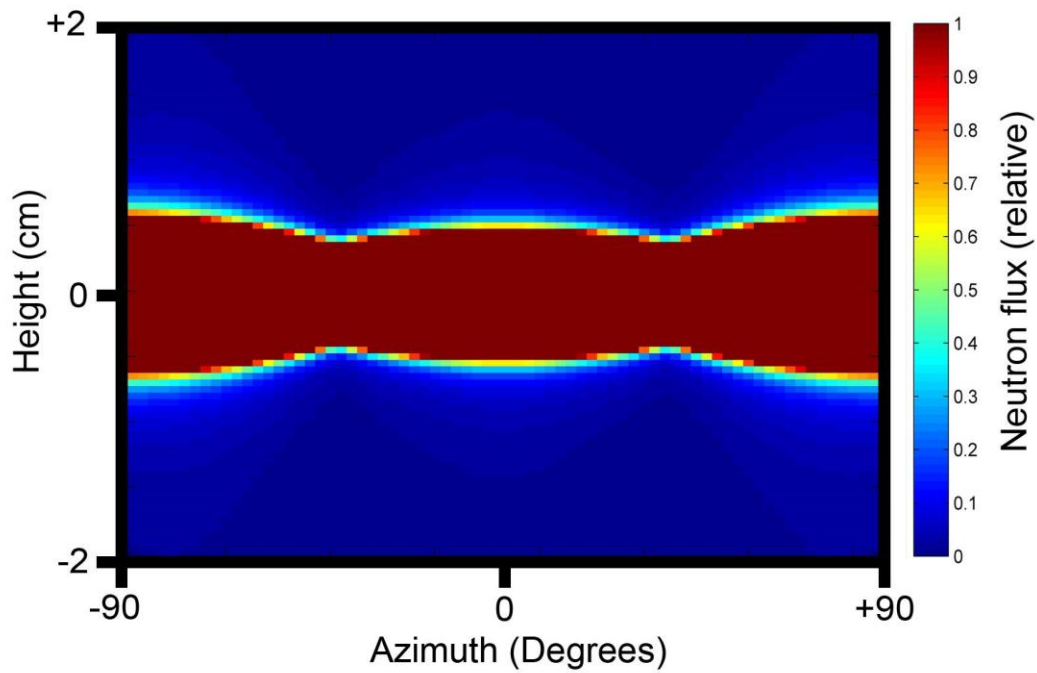


Fig. 3

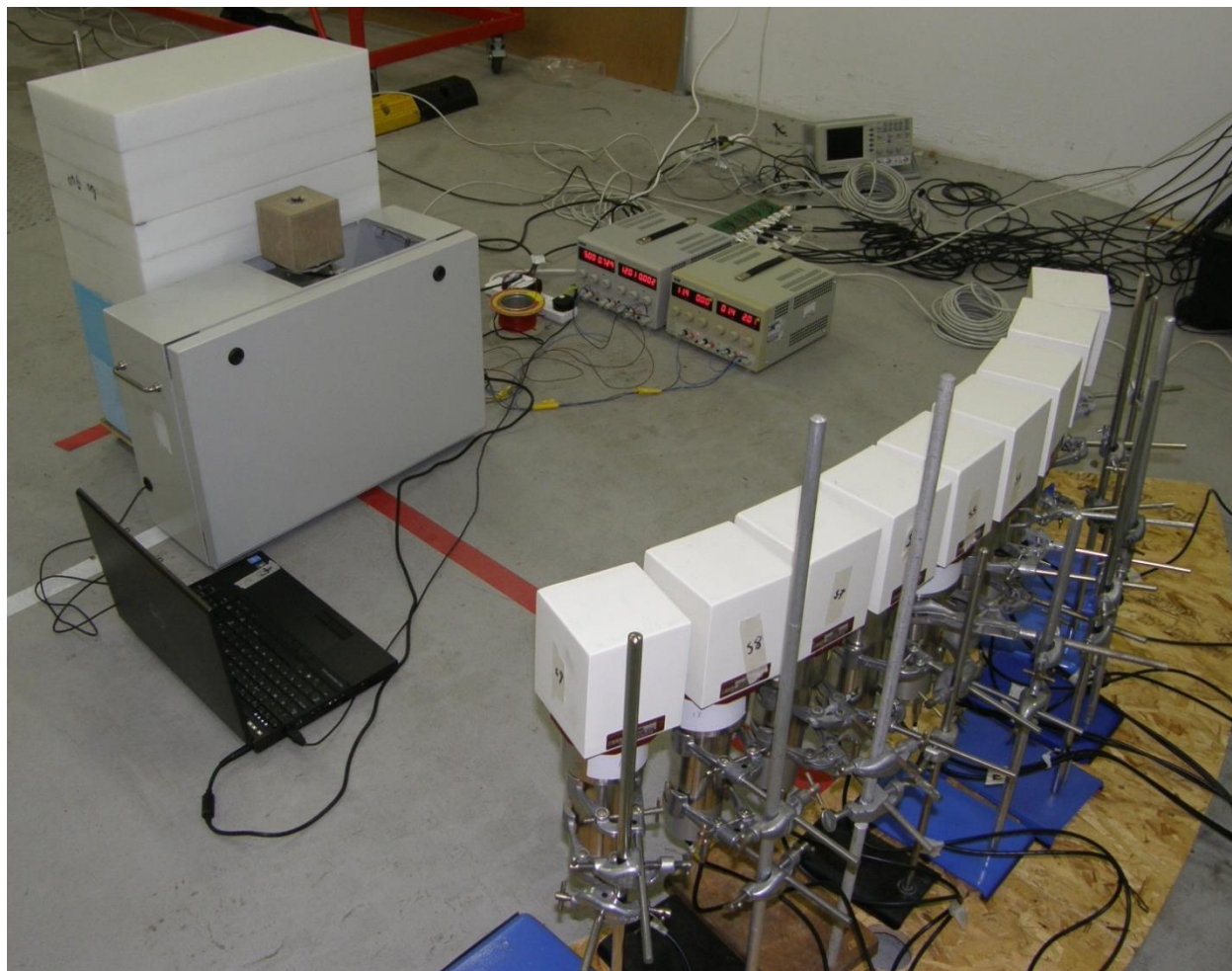


Fig. 4

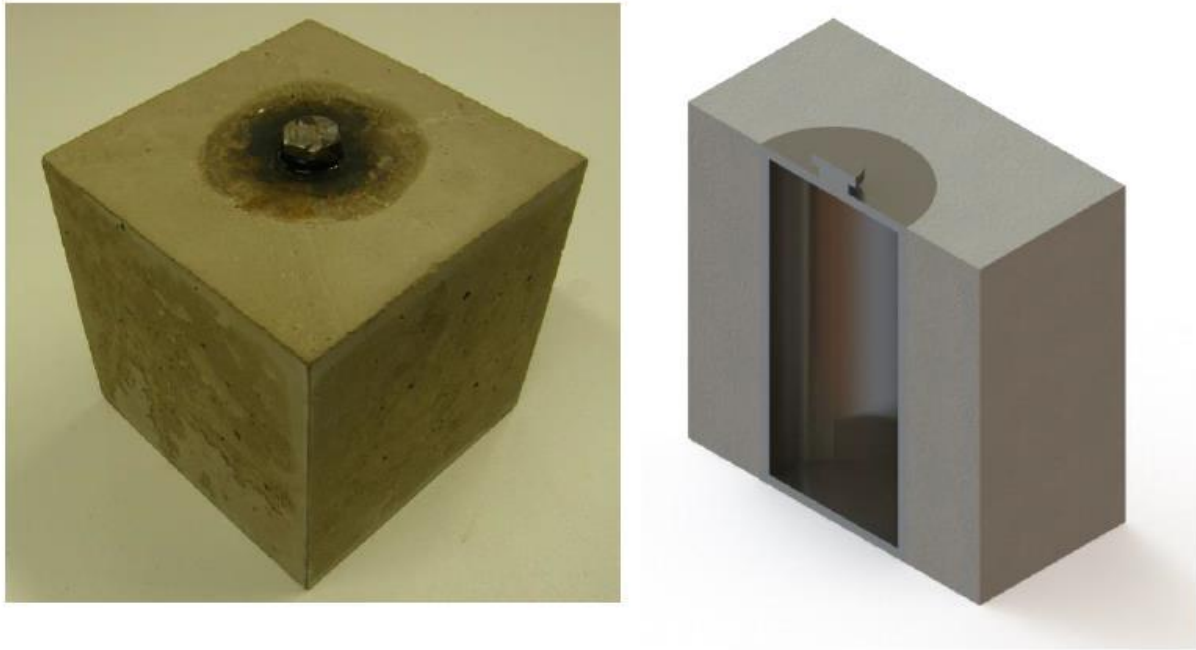


Fig. 5a

Accepted manuscript

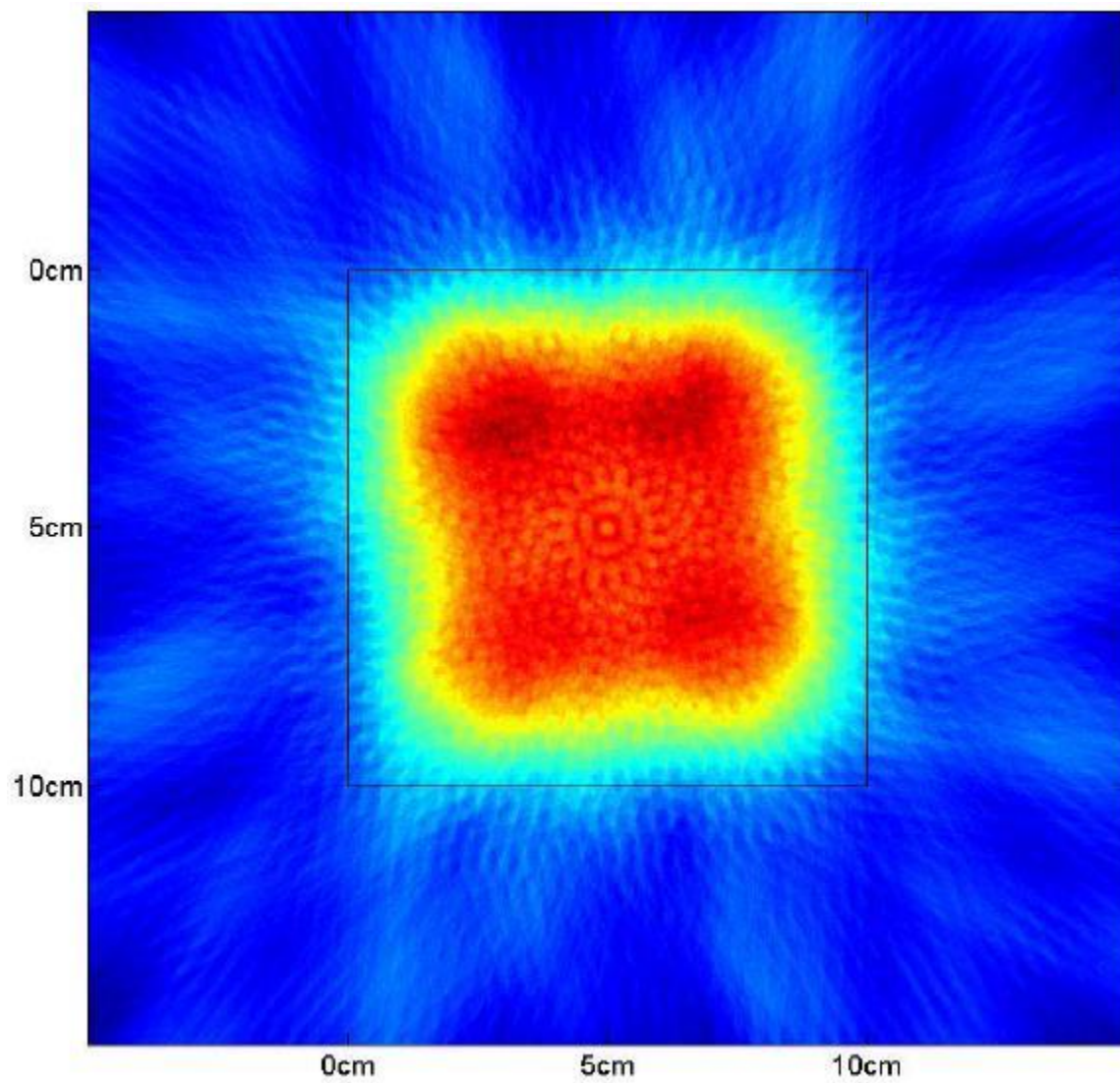


Fig. 5b

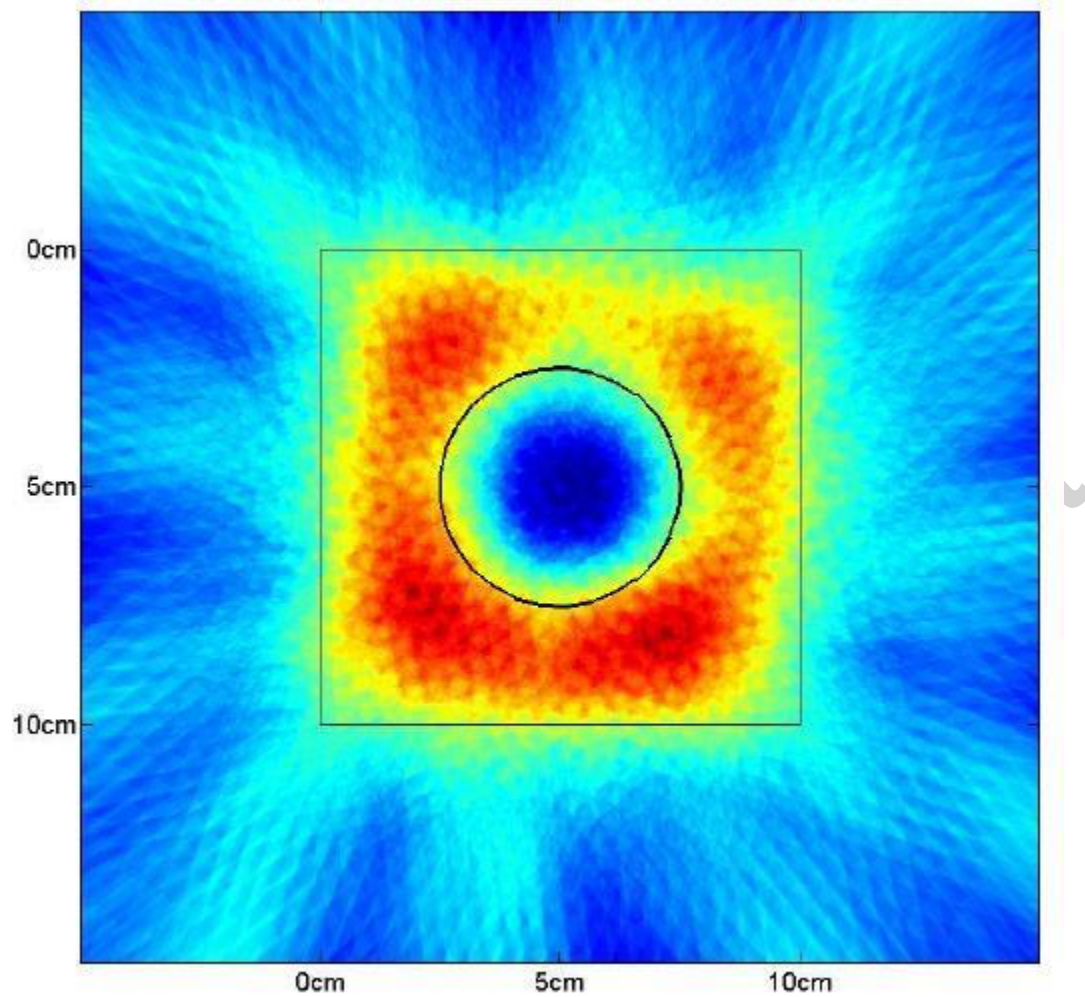


Fig. 6

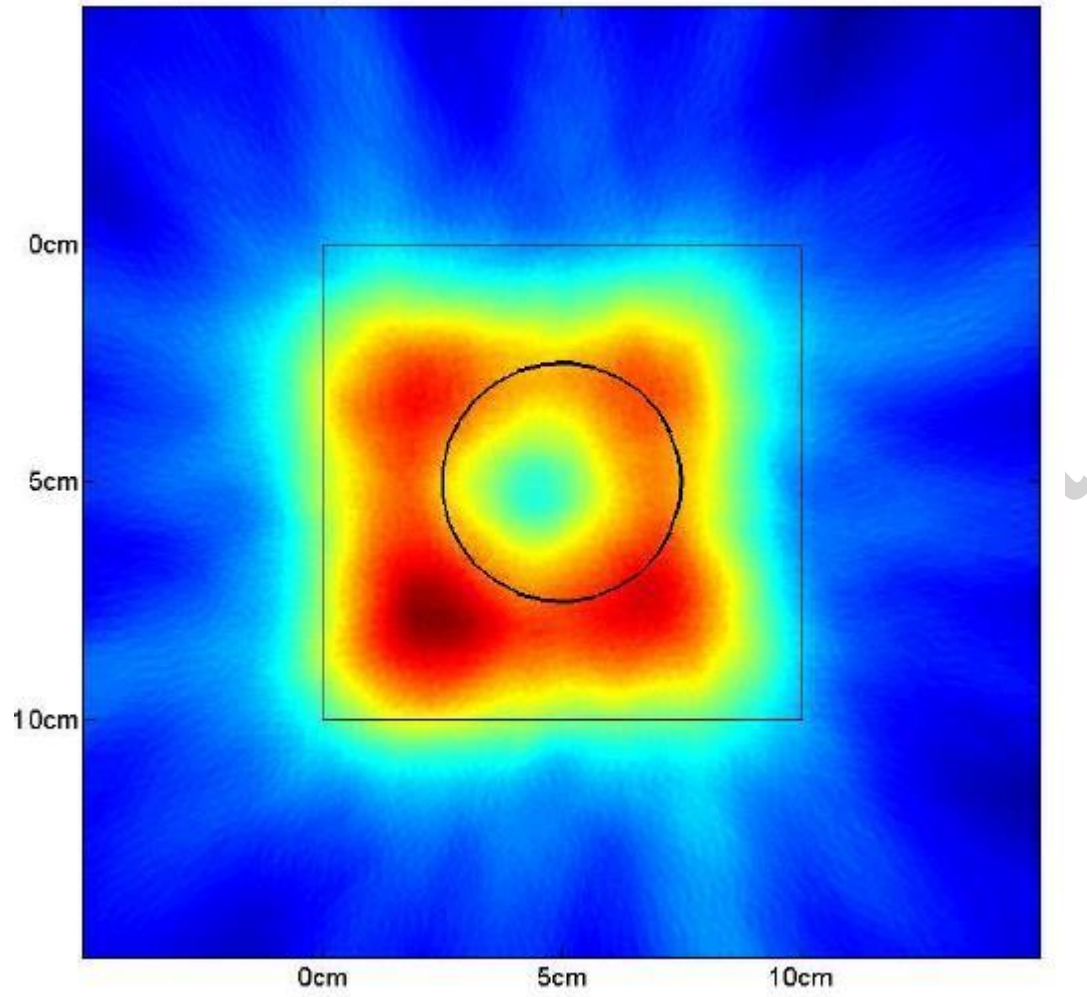


Fig. 7a

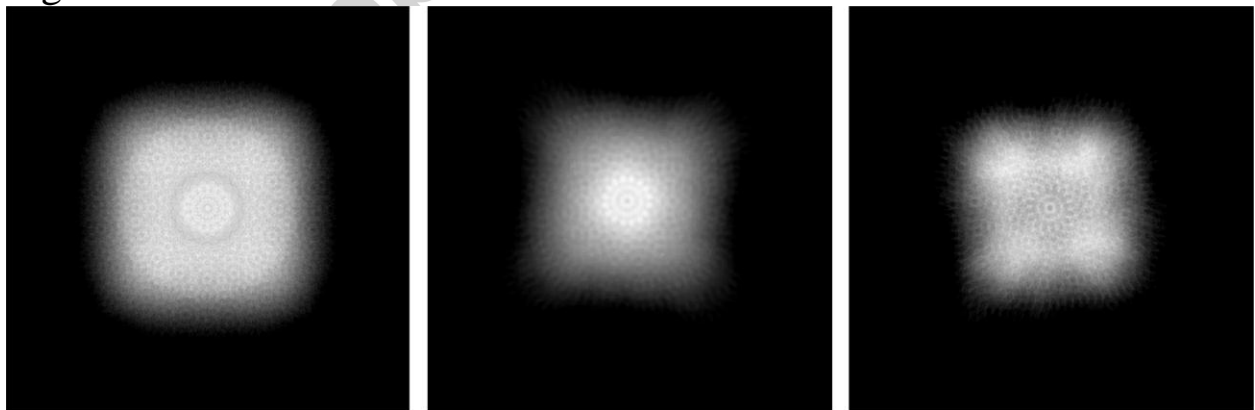


Fig. 7b

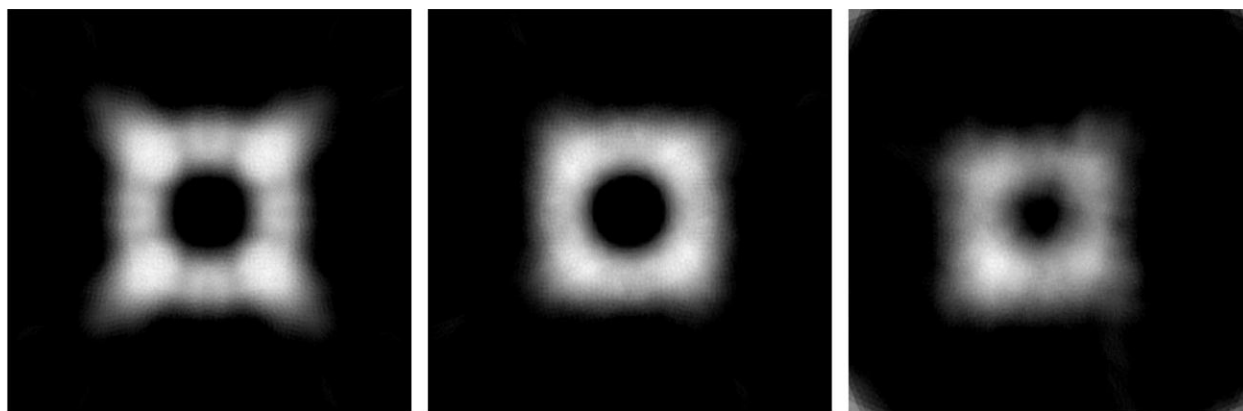


Fig. 8a

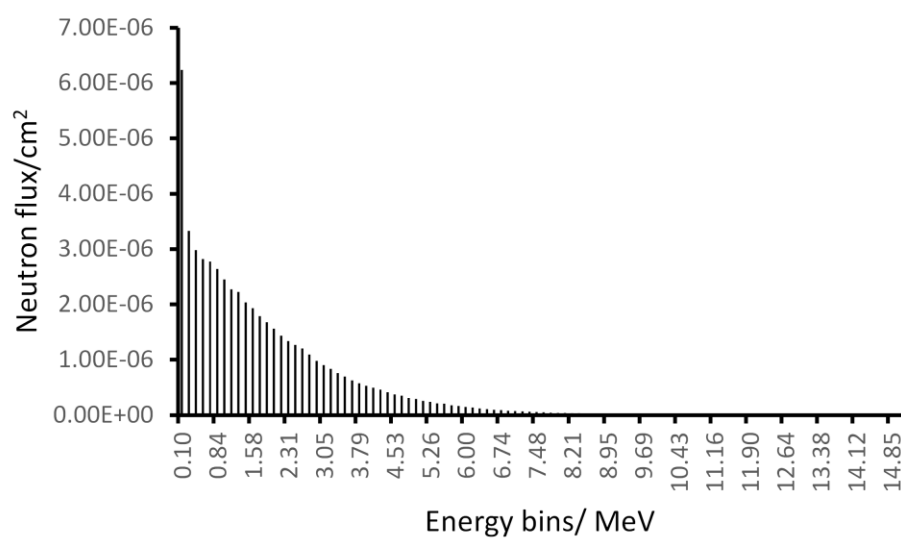


Fig. 8b

